

Article

Magnetic and Structural Properties of Barium Hexaferrite Nanoparticles Doped with Titanium

Abdul Raouf Al Dairy¹, Lina A. Al-Hmoud^{2,*}  and Heba A. Khatatbeh¹

¹ Department of Physics, Yarmouk University, Irbid 21163, Jordan; abedali@yu.edu.jo (A.R.A.D.)
heba.haboush92@yahoo.com (H.A.K.)

² Department of Electrical Power Engineering, Yarmouk University, Irbid 21163, Jordan

* Correspondence: lina.hmoud@yu.edu.jo; Tel.: +962-7-9018-4875

Received: 6 May 2019; Accepted: 24 May 2019; Published: 28 May 2019



Abstract: Samples of Barium Hexaferrite doped with Titanium $\text{BaFe}_{12-x}\text{Ti}_x\text{O}_{19}$ with ($x = 0.0, 0.2, 0.4, 0.6, 0.8, 1.0$) were synthesized by the sol-gel auto-combustion technique. The powdered samples were divided into two parts, one sintered at 850 °C and another sintered 1000 °C for 1 h and samples were characterized by different experimental techniques. The XRD patterns confirmed the presence of M-type hexaferrite phase. The sizes of the crystallites were calculated by the Scherer equation, and the sizes were in the range of 27–42 nm. Using the hysteresis loops, the saturation magnetization M_s , remanence (M_r), the relative ratio (M_r/M_s), and the coercivity (H_c) were calculated. The study showed that the saturation magnetization (M_s) and remanence (M_r) decreased with increasing titanium concentration and were in the range from 44.65–17.17 emu/g and 23.1–7.7 emu/g, respectively. The coercivity (H_c) ranged between 0.583 and 4.51 (kOe). The magnetic properties of these Barium Hexaferrite doped with Titanium indicated that they could be used in the recording equipment and permanent magnets.

Keywords: Barium hexaferrite; titanium; hysteresis; X-ray diffraction; permanent magnet applications

1. Introduction

There are vast numbers of applications based on magnetic materials and as a result of that; our lives have improved. They are used in the fabrication of many types of equipment and have a major role in the advancement of technological and industrial products. The types of magnetic materials, according to their magnetic behavior, are one of five types; Diamagnetic, Paramagnetic, Ferromagnetic, Antiferromagnetic, and Ferrimagnetic materials [1–3]. Magnetic ferrites, first discovered in the 1950s, are ceramics made from iron oxides with one or more additional metals chemically added [4,5]. These ferrites had been considered very highly valuable electronic materials for many decades. The ferrite compounds have a cubic structure, but there is also a group of ferrites with a hexagonal crystal structure, known as hexaferrites [6]. There was an increasing degree of interest in hexaferrites, and it is still growing today. They have been massively produced and became important materials; commercially and technologically used in many electrical systems, such as permanent magnets, magnetic recording and data storage devices [6,7].

The hexaferrites are complex oxide systems with a general chemical formula $\text{AO-Fe}_2\text{O}_3\text{-MO}$, where A is a large divalent cation, i.e., Ba, Sr, Ca, and M are a small divalent cation, i.e., Mn, Fe, Co, Ni, Cu, and Zn. They can be classified on the basis of their chemical composition and the A–M combination and the crystal structure into six fundamental, structural types: M, W, Y, X, U, and Z [8–13].

The ferromagnetic and ferromagnetic types show nonlinear relation between the magnetization M of the compound and the applied H . The hysteresis loop depicts the behavior of the magnetization M of the sample with the variation of the applied field H . As H increases, the magnetization increases

up to its highest value; this defines an important characteristic parameter of the material called the saturation magnetization M_s at high enough applied fields. The value of the field needed to reach the saturation magnetization depends on the nature of the material, method of preparation, and other intrinsic and extrinsic parameters. The magnetization retains a value even at zero applied fields called the remnant magnetization or the remanence M_r . This parameter has particular importance in the case of permanent magnets production because it defines the magnetization of a magnet in the absence of an applied external field. The size of the opposite field needed to reduce M to zero is called the coercivity H_c . The value of the coercive field, the coercivity, defines the so-called magnetic hardness of the magnetic material [14].

Many research groups prepared these ferrites and investigated the effect of the dopants on the magnetic properties of such M-type magnetic hexaferrites [15–33]. The hexaferrites are of great interest for applications in the microwave technology and others. S.V. Trukhanov et al. studied the effect of gallium doping on the properties of barium hexaferrite, $\text{BaFe}_{12-x}\text{Ga}_x\text{O}_{19}$ ($x \leq 1.2$), prepared by the ceramic technology method [34,35]. They showed that the unit cell monotonically decreases with increasing x and these Ga doped hexaferrites can effectively absorb high-frequency electromagnetic radiation. The maximum of the real part of permeability depends on the level of substitution by titanium cations and it is located in the region of 5–6 GHz. For gallium-substituted hexaferrites, the real part of permittivity decreases more slowly at low frequencies and almost monotonically with concentration. In last case, the real and imaginary parts of the permeability have a peak in the region of 49–51 GHz, which is determined by the level of diamagnetic substitution. Researchers have prepared $(\text{BaFe}_{11.9}\text{Al}_{0.1}\text{O}_{19})_{1-x}(\text{BaTiO}_3)_x$ with $x = 0, 0.25, 0.5, 0.75,$ and 1 bicomponent compounds using the ceramic technique [36]. The researchers reported that these hexaferrites exhibited ferroelectricity at room temperature and the coercive field was lower due to the contribution of the microstructure-dependent shape anisotropy to the magnetic anisotropy energy and the behavior of these samples was discussed based on the grain size, density, and porosity. The magnetic and dipole moments in $\text{BaFe}_{12-x}\text{In}_x\text{O}_{19}$ hexaferrites were studied by S. V. Trukhanov group [37]. These indium doped samples were prepared by solid reaction method as published by coworkers of the same group before [38]. The samples were studied by high resolution neutron powder diffraction and vibrating sample magnetometry in the temperature range of 4–730 K. They showed that spontaneous polarization was established due to the displacement of $\text{Fe}^{3+}(\text{In}^{3+})$ cations and the appearance of nonzero electric dipole moment, which causes the formation of the z-component of the spontaneous polarization. The crystal structure and magnetic properties of $\text{BaFe}_{12-x}\text{Me}_x\text{O}_{19}$ ($\text{Me} = \text{In}^{3+}$ or Ga^{3+} and $x = 0.1–1.2$) solid solutions were studied using the time-of-flight neutron diffraction method [39]. The workers reported that the electric field-induced polarization was observed in these barium hexaferrite solid solutions at room temperature. Using the Gorter's model, the researchers found that the magnetic moments of iron ions were oriented along the hexagonal axis which is the easy axis of magnetization. The previously mentioned works of S.V. Trukhanov and co-workers proved that the magnetoelectric characteristics of M-type hexaferrites fabricated by a modified ceramic technique can be more advanced than those for the well-known room temperature BiFeO_3 orthoferrite multiferroic.

The main goal of this project was to study the effect of Titanium substitution on the magnetic and structural properties of the barium hexaferrites prepared according to the formula $\text{BaFe}_{11.9}\text{Ti}_x\text{O}_{19}$ with $x = 0.0, 0.2, 0.4, 0.6, 0.8, 1.0$.

2. Experimental Techniques

A number of ferrite samples $\text{BaFe}_{12-x}\text{Ti}_x\text{O}_{19}$ with ($x = 0.0, 0.2, 0.4, 0.6, 0.8, 1.0$) were prepared by using the sol-gel auto combustion technique. The chemicals used for the preparation of the samples were $\text{Fe}(\text{NO}_3)_3$, $\text{Ba}(\text{NO}_3)_2$, and TiCl_3 and were dissolved in 100 ml of de-ionized water. Citric acid was added to the solution, and the molar ratio for the metallic mixture to acid was kept at 3:1 [33]. Using a hot plate and continuous stirring, the solution was heated up to a temperature of 80 °C. A solution of ammonia was added to the mixture to reach a pH value of 8.0. The solution was then heated slowly to

450 °C for several hours until a viscous brown gel mixture is formed. The gel was heated further to a temperature of 550 °C and the gel ignited and was burned out completely and formed a fluffy brown colored powder. This powder was divided into two samples, using a furnace one sample was sintered at 850 °C and the second sample was sintered at 1000 °C each for a period of one hour.

The structure of the samples was studied using X-ray powder diffraction (with Cu- K_{α} radiation $\lambda = 1.5405 \text{ \AA}$). Infrared spectroscopy was used to ensure the formation of M-type hexaferrite phase. The scanning electron microscope was used to study the microstructure of samples. Finally, the magnetic properties were studied at room temperature using a Vibrating Sample Magnetometer.

3. Results and Discussion

Figure 1 shows the XRD pattern for $\text{BaFe}_{12}\text{O}_{19}$ and the XRD patterns for doped $\text{BaFe}_{12-x}\text{Ti}_x\text{O}_{19}$ samples sintered at 850 °C, while Figure 2 shows the XRD pattern for $\text{BaFe}_{12}\text{O}_{19}$ and those patterns for doped $\text{BaFe}_{12-x}\text{Ti}_x\text{O}_{19}$ samples sintered at 1000 °C. It is clear that the XRD pattern for the $\text{BaFe}_{12}\text{O}_{19}$ (i.e., $x = 0$) as the prepared sample is consistent with the standard pattern (JPCDS #: 00-043-0002) for BaM compound but with a higher percentage of that phase at the higher sintering temperature. This leads to the conclusion that the samples must be sintered at temperatures even higher than 1000 °C. As seen from Figure 2, the patterns indicated the presence of $\alpha\text{-Fe}_2\text{O}_3$ in samples sintered at 1000 °C as seen from the peak at 33.1 degree and other lower peaks at 24.2, 49.4, and 54 degree and the content of $\alpha\text{-Fe}_2\text{O}_3$ changes with x and was the highest for $x = 0.6$. It is also clear from peaks at 53.2 and 61.8 degree that there are traces of FeTiO_3 oxide and the peak at 28.8 degree indicated a presence of a small trace of BaTiO_3 .

The Scherrer formula was then used to calculate the average crystallite sizes for the samples:

$$D = \frac{k\lambda}{\beta \cos \theta}. \quad (1)$$

Here, D is the average crystallite size, K is called the Scherrer's constant and is taken equal to 0.89 for the hexaferrite, λ is the x-ray wavelength and equals 1.5405 \AA , β is the width of the peak at half maximum and is measured in radians, and θ is the position of the peak. Using several peaks, the average crystallite size for all samples was calculated; the results and calculations are summarized in Tables 1 and 2.

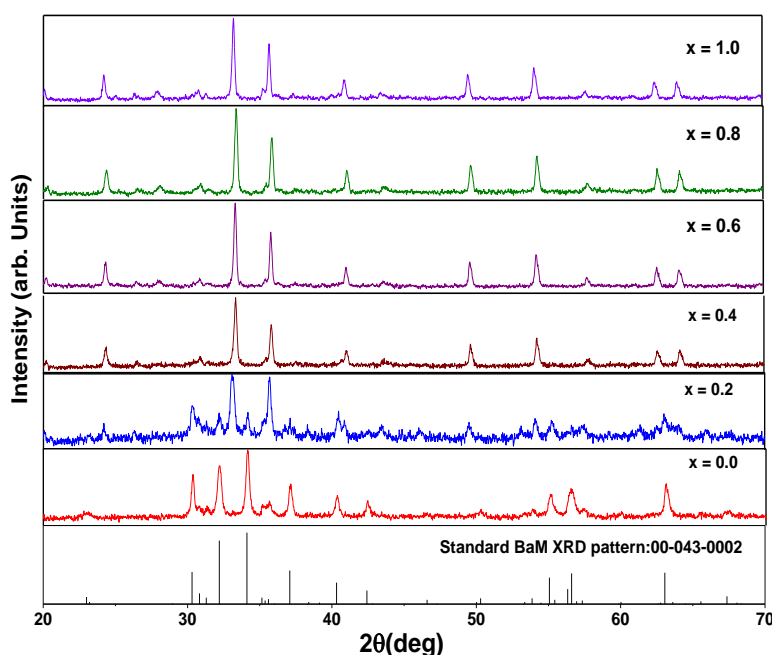


Figure 1. XRD patterns for $\text{BaFe}_{12-x}\text{Ti}_x\text{O}_{19}$ samples with ($x = 0.0\text{--}1.0$) sintered at 850 °C for 1 h and shown the standard pattern of $\text{BaFe}_{12}\text{O}_{19}$ (file no.: 043-0002).

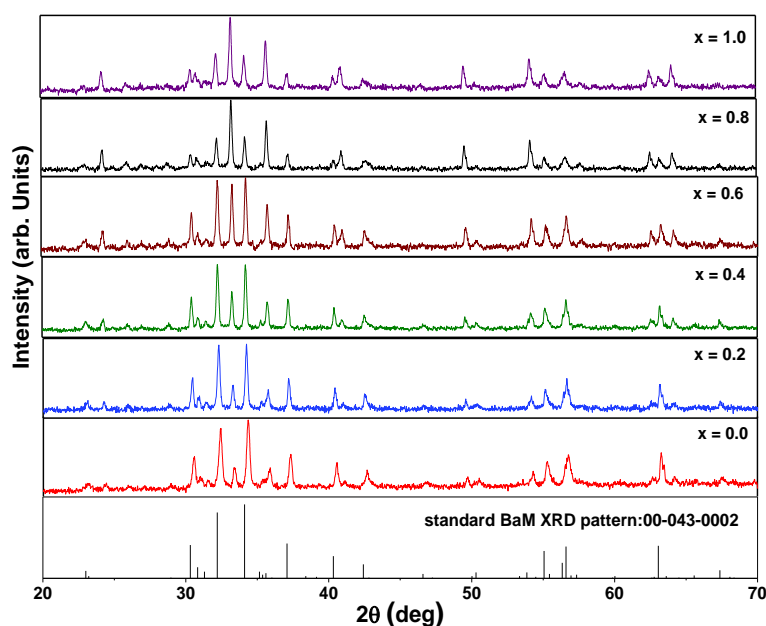


Figure 2. XRD patterns $\text{BaFe}_{12-x}\text{Ti}_x\text{O}_{19}$ samples with ($x = 0.0$ – 1.0) sintered at $1000\text{ }^\circ\text{C}$ for 1 h and shown the standard XRD pattern of $\text{BaFe}_{12}\text{O}_{19}$ (file no.: 043-0002).

The average crystallite sizes were found to be in the range of (27–36) nm for samples sintered at $850\text{ }^\circ\text{C}$, and the average crystallite sizes for samples sintered at $1000\text{ }^\circ\text{C}$ were found to be in the range of (35–41.5) nm. This may lead us to conclude that Ti substitution improved the BaM phase crystallinity especially at the sintering temperature of $1000\text{ }^\circ\text{C}$.

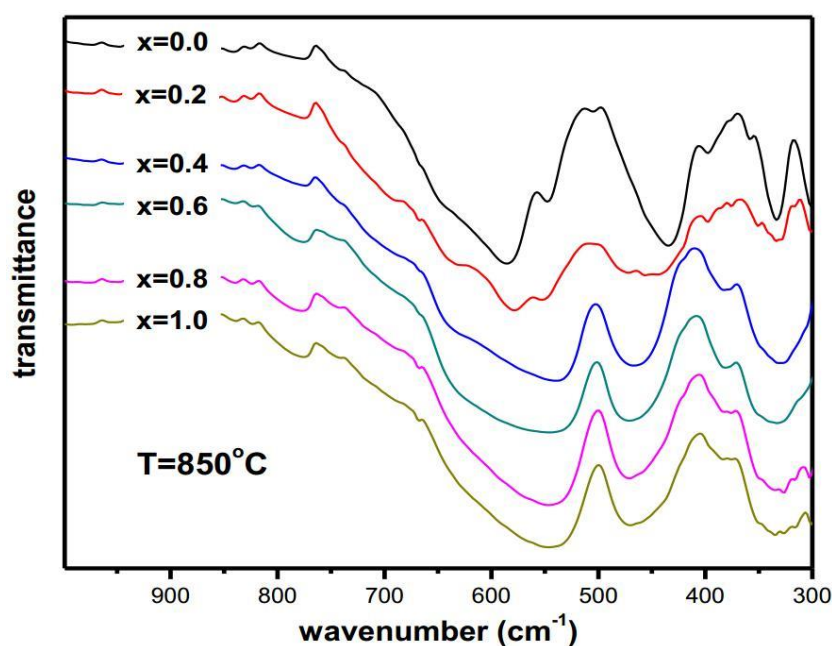
Table 1. The calculated average crystallite sizes for the system $\text{BaFe}_{12-x}\text{Ti}_x\text{O}_{19}$ with ($x = 0.0$ – 1.0) sintered at $T = 850\text{ }^\circ\text{C}$.

Sample	(2 θ)-Position (Degrees)	Size (nm)	Average Size (nm)
$\text{BaFe}_{12}\text{O}_{19}$ ($x = 0.0$)	32.19	24.8	27.2
	34.14	29.3	
	37.1	29.6	
	40.33	27	
	55.1	25.3	
$\text{BaFe}_{11.8}\text{Ti}_{0.2}\text{O}_{19}$ ($x = 0.2$)	33.1	27.3	30.3
	35.67	33	
	49.51	25.4	
	54.1	35.3	
$\text{BaFe}_{11.6}\text{Ti}_{0.4}\text{O}_{19}$ ($x = 0.4$)	33.3	34.1	34
	35.8	35.9	
	49.65	33.3	
	54.26	32.7	
$\text{BaFe}_{11.4}\text{Ti}_{0.6}\text{O}_{19}$ ($x = 0.6$)	33.31	39	36.5
	35.79	41	
	49.69	34.6	
	54.24	31.5	
$\text{BaFe}_{11.2}\text{Ti}_{0.8}\text{O}_{19}$ ($x = 0.8$)	33.39	34.2	34
	35.86	35.9	
	49.7	33.3	
	54.3	32.7	
$\text{BaFe}_{11.0}\text{Ti}_{1.0}\text{O}_{19}$ ($x = 1.0$)	33.31	39	36.3
	35.69	41.3	
	49.54	34.6	
	54.15	30.4	

Table 2. The calculated average crystallite sizes for the system $\text{BaFe}_{12-x}\text{Ti}_x\text{O}_{19}$ with ($x = 0.0$ – 1.0) sintered at $T = 1000^\circ\text{C}$.

Sample	(2 θ)-Position (Degrees)	Size (nm)	Average Size (nm)
$\text{BaFe}_{12}\text{O}_{19}$ ($x = 0.0$)	32.4	30.3	34.9
	34.34	41	
	40.55	36.4	
$\text{BaFe}_{11.8}\text{Ti}_{0.2}\text{O}_{19}$ ($x = 0.2$)	55.31	31.7	38.7
	32.29	38.9	
	34.23	41.1	
	40.44	41.9	
	55.1	32.8	
$\text{BaFe}_{11.6}\text{Ti}_{0.4}\text{O}_{19}$ ($x = 0.4$)	32.26	43.1	41.5
	34.22	45.7	
	40.42	46.5	
	55.19	30.6	
	32.29	43	
$\text{BaFe}_{11.4}\text{Ti}_{0.6}\text{O}_{19}$ ($x = 0.6$)	34.27	45.7	41
	40.48	39.9	
	54.23	35.3	
	33.27	45.6	
$\text{BaFe}_{11.2}\text{Ti}_{0.8}\text{O}_{19}$ ($x = 0.8$)	34.24	43.3	40.5
	40.96	36.5	
	54.19	36.7	
	33.23	43.1	
$\text{BaFe}_{11.0}\text{Ti}_{1.0}\text{O}_{19}$ ($x = 1.0$)	35.7	41.3	38
	40.93	32.2	
	54.19	35.3	

To prove the presence of M-type hexaferrite phase, Infra-Red (IR) analysis was used because the IR- spectra can point to its presence. The samples were mixed with 0.05% KBr in order to get an acceptable resolution of the compound bands. IR spectra of the as-prepared samples were obtained with a wave number varying between 300 cm^{-1} to 1000 cm^{-1} and the results are summarized in Figures 3 and 4 for the two sintering temperatures, respectively.

**Figure 3.** Infra-Red (IR) spectra of $\text{BaFe}_{12-x}\text{Ti}_x\text{O}_{19}$ sintered at $T = 850^\circ\text{C}$.

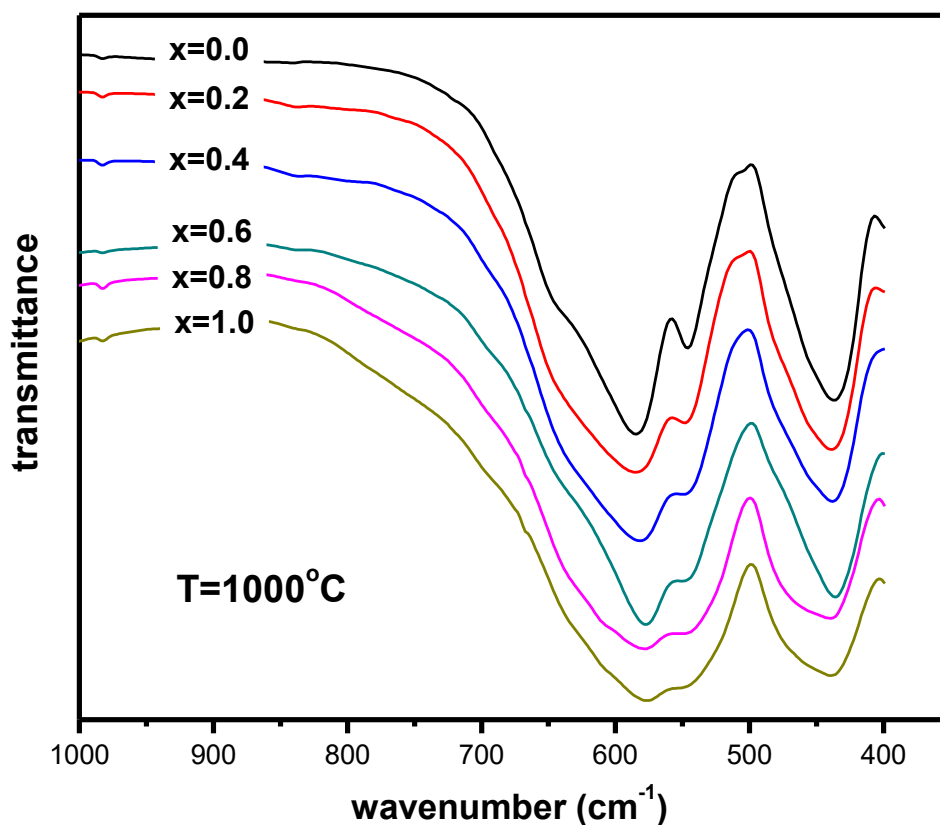


Figure 4. IR spectra of $\text{BaFe}_{12-x}\text{Ti}_x\text{O}_{19}$ sintered at $T = 1000\text{ }^\circ\text{C}$.

As seen from Figures 3 and 4, the IR spectra of the sintered samples have absorption bands at wave numbers in the range $430\text{--}590\text{ cm}^{-1}$, which are characteristic to the formation of ferrites. The peaks were clearer for those samples sintered at $1000\text{ }^\circ\text{C}$. The peak at about 430 cm^{-1} is due to bending of the absorption bands of the metal-oxygen and that at about 590 cm^{-1} is due stretching of these bands.

Figure 5 shows an SEM image for one of the samples, namely $\text{BaFe}_{12-x}\text{Ti}_x\text{O}_{19}$ (with $x = 0.2$), which was sintered at $T = 1000\text{ }^\circ\text{C}$. It shows that grains are ultrafine and almost have homogeneous distribution. The image also shows that the platelets have sizes in the range of 200 nm to 500 nm .

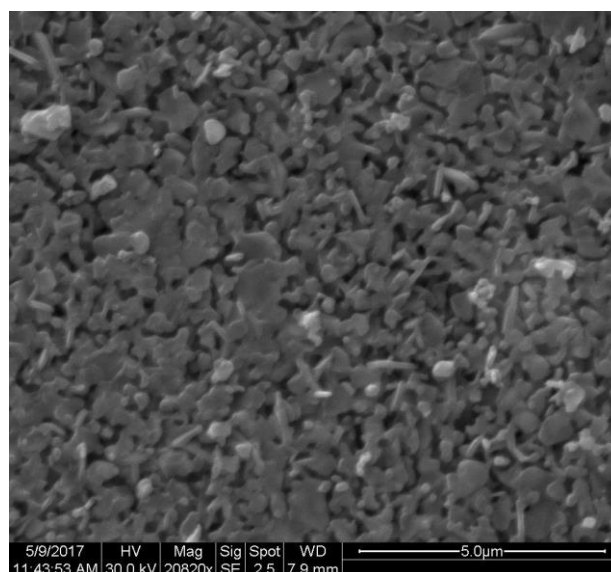


Figure 5. SEM image for $\text{BaFe}_{12-x}\text{Ti}_x\text{O}_{19}$ ($x = 0.2$) sample sintered at $T = 1000\text{ }^\circ\text{C}$.

Based on X-ray results and IR data, we believe that samples are improved if heat-treated at 1000 °C.

We studied only magnetic properties for samples sintered at 1000 °C. Magnetic measurements were carried out at room temperature by a VSM with applied field between 0 and 10 kOe. The group of hysteresis loops (HL) for all samples is shown in Figure 6. The loops do indicate that all the samples are indeed hard magnetic materials. The values of remanence magnetization and coercive field for each sample were read directly from graphs of loops. Since it is expected that samples have high magnetic anisotropy, we used the law of approach to saturation (LAS) to calculate the saturation magnetization. This is simply found by plotting M versus $1/H^2$ for values taken from high field region and all samples gave perfect straight linear graphs. The intercept of that line is equal to the saturation magnetization.

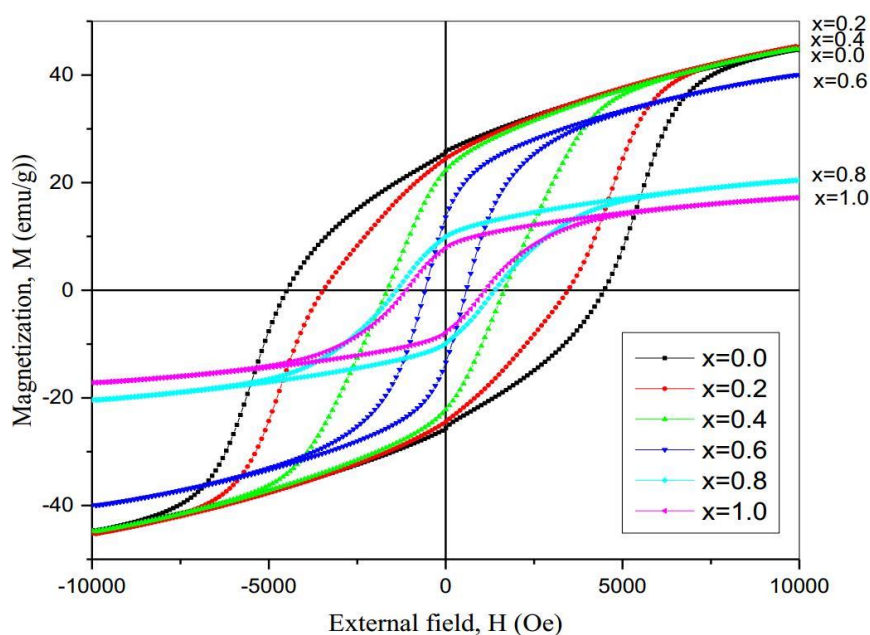


Figure 6. Hysteresis loops for the samples $\text{BaFe}_{12-x}\text{Ti}_x\text{O}_{19}$ ($x = 0.0 - 1.0$) sintered at 1000 °C.

Table 3 shows summary of the calculated values for the saturation magnetization, the remanence magnetization, the reduced magnetization, and the coercivity.

Table 3. The saturation magnetization, remanence magnetization, reduced remnant magnetization and coercive field for the system $\text{BaFe}_{12-x}\text{Ti}_x\text{O}_{19}$ ($x = 0.0-1.0$).

x	M_s (emu/g)	M_r (emu/g)	M_{rs} (emu/g)	H_c (kOe)
0.0	44.65	23.0606	0.5165	4.51
0.2	45.24	19.7474	0.4365	3.4557
0.4	44.83	19.5835	0.4368	1.6554
0.6	39.99	12.9342	0.3234	0.583
0.8	20.39	9.5829	0.47	1.385
1.0	17.17	7.7163	0.4494	1.11455

The saturation magnetization shows inverse relation titanium concentration. The partial substitution of Fe by titanium ions in these hexaferrites has affected the values of M_s , which depends on the amount of Ti ions diffusing into the BaM crystal in which Ti^{3+} ions partially replace Fe^{3+} . However, the higher the Ti concentration results in lower M_s because other phases are then formed as was concluded from XRD data.

Hard ferrites typically have a high value of M_r , which is about 50% of the saturation magnetization (M_s), therefore the reduced remnant magnetization ($M_{rs} = M_r/M_s$) must be nearly 0.5, and this is

true for samples consisting of single-domains and random orientations of grains [32]. Table 3 shows that the values of M_{rs} are very close to 50%. The coercive field, H_c , for the samples varied with Ti concentration and it ranged between 0.6 and 4.5 kOe as can be seen in Table 3. A plot of M_s and H_c versus the concentration of titanium is shown in Figure 7.

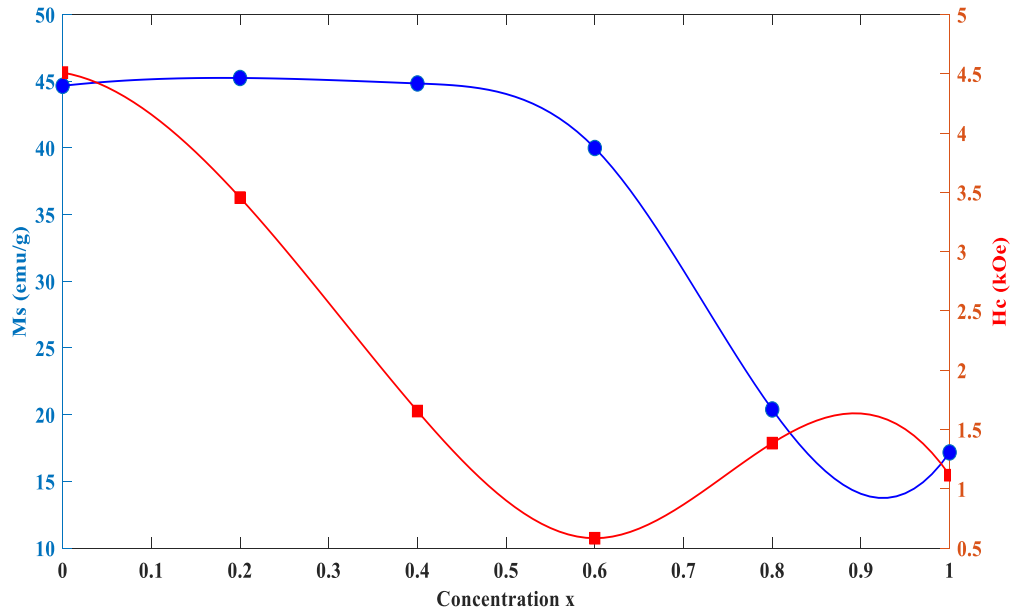


Figure 7. Saturation magnetization and coercive field versus Ti concentration.

We calculated the average paramagnetic behavior for each sample by approximating the loop by a straight line as shown in Figure 8. Of course, this behavior is correct only for shallow applied fields, but we found that there is a general trend in these samples that can be depicted by the slopes of these lines. Slopes of these lines are listed in Table 4. The slopes are related to the magnetic susceptibility and increased slowly by increasing the concentration up to $x = 0.6$ and then decreases to half its value after that.

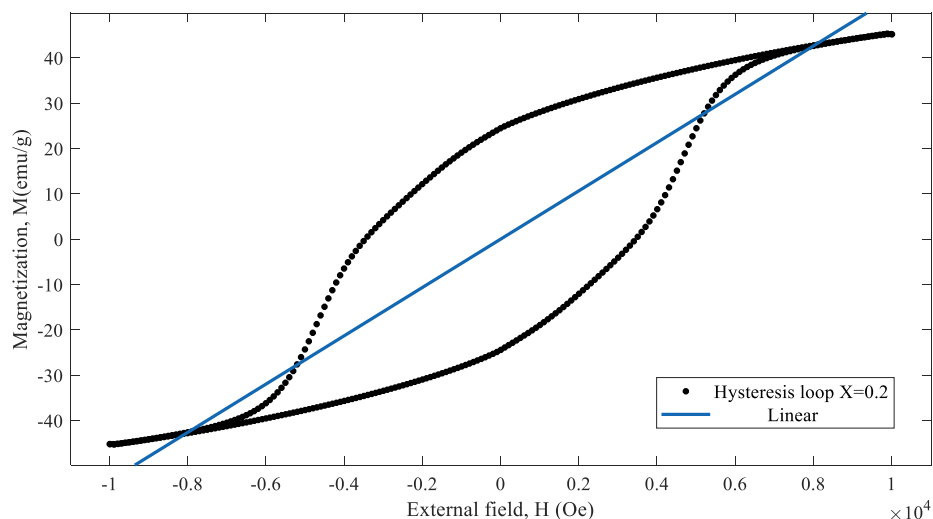
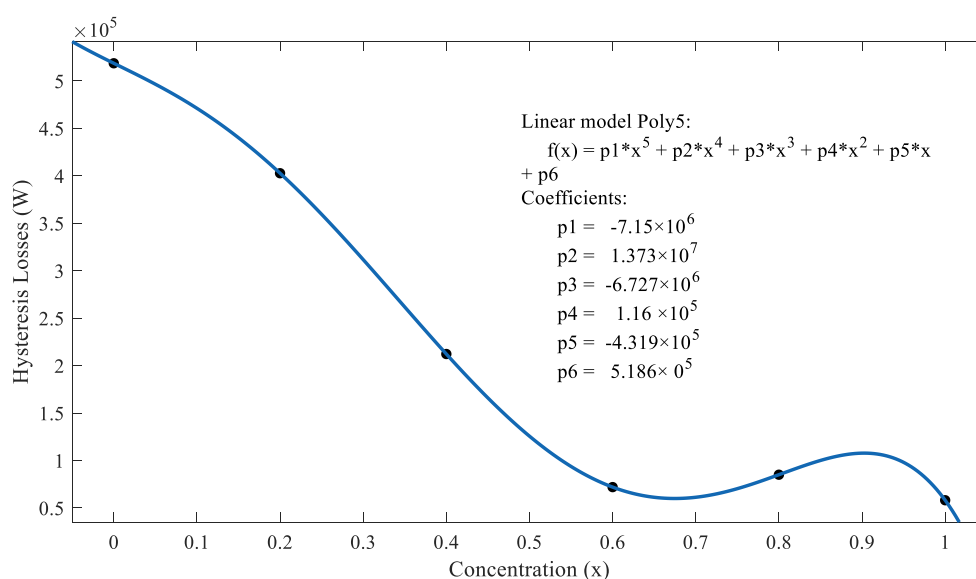


Figure 8. The hysteresis loop for the system $BaFe_{12-x}Ti_xO_{19}$ ($x = 0.2$) approximated by a straight line.

Table 4. The slope and hysteresis losses (in W) for the system $\text{BaFe}_{12-x}\text{Ti}_x\text{O}_{19}$ ($x = 0.0\text{--}1.0$).

Concentration (x)	Slope	Hysteresis Losses (W)
0.0	0.004908	518,580
0.2	0.005326	402,700
0.4	0.00571	212,180
0.6	0.005252	71,914
0.8	0.002623	84,982
1.0	0.002229	58,080

We also calculated hysteresis losses for each sample and the calculated values are listed in Table 4. It is clear from the values of losses that Ti concentration could be a scaling factor for magnetic energy stored when these materials are used in components of electromagnetic devices. This behavior is displaced in Figure 9. Losses are significant and almost linear for $x < 0.6$.

**Figure 9.** Hysteresis losses (in W) $\text{BaFe}_{12-x}\text{Ti}_x\text{O}_{19}$ ($x = 0.0\text{--}1.0$) sintered at $1000\text{ }^\circ\text{C}$.

4. Conclusions

A group of $\text{BaFe}_{12-x}\text{Ti}_x\text{O}_{19}$ samples with ($x = 0.0\text{--}1.0$) were prepared by sol-gel-auto combustion method and were sintered at $850\text{ }^\circ\text{C}$ and $1000\text{ }^\circ\text{C}$ for 1 h in air. The XRD data and IR data analysis confirmed the presence of M type phase of the hexaferrite in these samples, and the higher sintering temperature showed an improvement of crystallinity. The average crystallite size for all samples was in the range of 27–42 nm. We believe that these are suitable to obtain the reasonable signal to noise ratio when used in a high-density recording medium. The values of saturation magnetization (M_s) and retentivity (M_r) calculated values decreased with increasing the Ti concentration, and this may result from particle size effects. The addition of titanium reduced the saturation magnetization from about 45 emu/g down to 17.2 emu/g. The rest of the magnetic properties that include coercivity, remanence magnetization, reduced remnant magnetization, and hysteresis losses suggest that these materials are beneficial in the components of electromagnetic devices that are used in recording technology and permanent magnets. We suggest that further work is needed to study the effect of sintering temperatures and very low controlled Ti concentrations. In addition, structural and magnetic studies at temperatures above and below room temperature using other techniques could be of great importance.

Author Contributions: Formal analysis, L.A.A.-H.; Methodology, H.A.K.; Supervision, A.R.A.D. All authors contribute equally to this manuscript.

Funding: This research received no external funding.

Acknowledgments: This research work was supported by the Deanship of Graduate Studies and Research, Yarmouk University, Irbid, Jordan; project 7/2017. We acknowledge the help of Prof. A. Hammoudeh in preparation of samples and IR data.

Conflicts of Interest: The authors declare no conflict of interest.

References

1. Gutfleisch, O.; Willard, M.A.; Bruck, E.; Chen, C.H.; Sankar, S.G.; Liu, J.P. Magnetic materials and devices for the 21st century: Stronger, lighter, and more energy efficient. *Adv. Mater.* **2011**, *23*, 821–842. [[CrossRef](#)]
2. Cullity, B.D.; Graham, C.D. *Introduction to Magnetic Materials*; John Wiley & Sons: New York, NY, USA, 2011.
3. Bini, R.A.; Marques, R.F.C.; Santos, F.J.; Chaker, J.A.; Jafellici, M., Jr. Synthesis and functionalization of magnetite nanoparticles with different amino-functional alkoxy silanes. *J. Magn. Magn. Mater.* **2012**, *324*, 534–539. [[CrossRef](#)]
4. Cocharadt, A. Recent ferrite magnet developments. *J. Appl. Phys.* **1966**, *37*, 1112–1115. [[CrossRef](#)]
5. Sugimoto, M. The past, present, and future of ferrites. *J. Am. Ceram. Soc.* **1999**, *82*, 269–280. [[CrossRef](#)]
6. Pullar, R.C. Hexagonal ferrites: A review of the synthesis, properties and applications of hexaferrite ceramics. *Prog. Mater. Sci.* **2012**, *57*, 1191–1334. [[CrossRef](#)]
7. Koutzarova, T.; Kolev, S.; Ghelev, C.; Grigorov, K.; Nedkov, I. Structural and magnetic properties and preparation techniques of nanosized M-type hexaferrite powders. In *Advances in Nanoscale Magnetism*; Springer: Berlin, Germany, 2009; pp. 183–203.
8. Maswadeh, Y.; Mahmood, S.H.; Awadallah, A.; Aloqaily, A.N. Synthesis and structural characterization of nonstoichiometric barium hexaferrite materials with Fe:Ba ratio of 11.5–16.16. In *IOP Conference Series: Materials Science and Engineering*; IOP Publishing Ltd.: Philadelphia, PA, USA, 2015.
9. Radwan, M.; Rashad, M.M.; Hessien, M.M. Synthesis and characterization of barium hexaferrite nanoparticles. *J. Mater. Process. Technol.* **2007**, *181*, 106–109. [[CrossRef](#)]
10. Martirosyan, K.S.; Galstyan, E.; Hossain, S.M.; Wang, Y.-J.; Litvinov, D. Barium hexaferrite nanoparticles: synthesis and magnetic properties. *Mater. Sci. Eng. B* **2011**, *176*, 8–13. [[CrossRef](#)]
11. Meng, Y.Y.; He, M.H.; Zeng, Q.; Jiao, D.L.; Shukla, S.; Ramanujan, R.V.; Liu, Z.W. Synthesis of barium ferrite ultrafine powders by a sol–gel combustion method using glycine gels. *J. Alloy. Compd.* **2014**, *583*, 220–225. [[CrossRef](#)]
12. Kouřil, K. Local structure of hexagonal ferrites studied by NMR. (2013). Available online: <https://www.researchgate.net> (accessed on 20 March 2019).
13. Wu, M. M-Type barium hexagonal ferrite films. In *Advanced Magnetic Materials Adv*; InTech Open: London UK, 2012.
14. Awadallah, A.M.; Sami, M. Effects of preparation conditions and metal ion substitutions for barium and iron on the properties of M-type barium hexaferrites. Ph.D. Research Proposal, The University of Jordan, Amman, Jordan, 2012. [[CrossRef](#)]
15. Zhang, H.; Zeng, D.; Liu, Z. The law of approach to saturation in ferromagnets originating from the magnetocrystalline anisotropy. *J. Magn. Magn. Mater.* **2010**, *322*, 2375–2380. [[CrossRef](#)]
16. Bsoul, I.; Mahmood, S.H. Magnetic and structural properties of BaFe_{12-x}Ga_xO₁₉ nanoparticles. *J. Alloy. Compd.* **2010**, *489*, 110–114. [[CrossRef](#)]
17. Awawdeh, M.; Bsoul, I.; Mahmood, S.H. Magnetic properties and Mössbauer spectroscopy on Ga, Al, and Cr substituted hexaferrites. *J. Alloy. Compd.* **2014**, *585*, 465–473. [[CrossRef](#)]
18. Packiaraj, G.; Panchal, N.R.; Jotania, R.B. Structural and Dielectric studies of Cu substituted Barium hexaferrite prepared by Sol-gel auto combustion technique. *Solid State Phenom.* **2014**, *209*, 102–106. [[CrossRef](#)]
19. Mahmood, S.H.; Aloqaily, A.N.; Maswadeh, Y.; Awadallah, A.; Bsoul, I.; Juwhari, H. Structural and magnetic properties of Mo-Zn substituted (BaFe_{12-4x}Mo_xZn_{3x}O₁₉) M-type hexaferrites. *Mater. Sci. Res. India* **2014**, *11*, 9–20. [[CrossRef](#)]
20. Haneda, K.; Hiroshi, K. Intrinsic coercivity of substituted BaFe₁₂O₁₉. *Japan. J. Appl. Phys.* **1973**, *12*, 355. [[CrossRef](#)]
21. Dushaq, G.H.; Mahmood, S.H.; Bsoul, I.; Juwhari, H.K.; Lahlouh, B.; Aldamen, M.A. Effects of molybdenum concentration and valence state on the structural and magnetic properties of BaFe_{11.6}Mo_xZn_{0.4-x}O₁₉ hexaferrites. *Acta Metall. Sin. (English Letters)* **2013**, *26*, 509–516. [[CrossRef](#)]

22. Ali, I.; Islam, M.U.; Awan, M.S.; Ahmad, M. Effects of Ga–Cr substitution on structural and magnetic properties of hexaferrite ($\text{BaFe}_{12}\text{O}_{19}$) synthesized by sol–gel auto-combustion route. *J. Alloy. Compd.* **2013**, *547*, 118–125. [[CrossRef](#)]
23. Wang, S.; Ding, J.; Shi, Y.; Chen, Y.J. High coercivity in mechanically alloyed $\text{BaFe}_{10}\text{Al}_2\text{O}_{19}$. *J. Magn. Magn. Mater.* **2000**, *219*, 206–212. [[CrossRef](#)]
24. Ali, I.; Islam, M.U.; Awan, M.S.; Ahmad, M.; Ashiq, M.N.; Naseem, S. Effect of Tb^{3+} substitution on the structural and magnetic properties of M-type hexaferrites synthesized by sol–gel auto-combustion technique. *J. Alloy. Compd.* **2013**, *550*, 564–572. [[CrossRef](#)]
25. Sharma, R.; Bisen, D.P.; Shukla, U.; Sharma, B.G. X-ray diffraction: a powerful method of characterizing nanomaterials. *Recent Res. Sci. Technol.* **2012**, *4*, 77–79.
26. Uvarov, V.; Popov, I. Metrological characterization of X-ray diffraction methods at different acquisition geometries for determination of crystallite size in nano-scale materials. *Mater. Charact.* **2013**, *85*, 111–123. [[CrossRef](#)]
27. Stuart, B.H. Experimental methods. In *Infrared Spectroscopy: Fundamentals And Applications*; John Wiley & Sons, Ltd.: Hoboken, NJ, USA, 2005; pp. 15–44.
28. Coates, J. Interpretation of infrared spectra, a practical approach. In *Encyclopedia of Analytical Chemistry*; John Wiley & Sons Ltd.: Chichester, UK, 2000; pp. 10815–10837.
29. Goldstein, J.; Yakowitz, H. *Practical Scanning Electron Microscopy: Electron and Ion Microprobe Analysis*; Springer: Boston, MA, USA, 1975.
30. Aravind, A. Synthesis and characterization of 3d-transition metals doped ZnO thin films and nanostructures for possible spintronic applications. Ph.D. Thesis, Cochin University of Science and Technology, Kerala, India, 2012.
31. Monshi, A.; Foroughi, M.R.; Monshi, M.R. Modified Scherrer equation to estimate more accurately nano-crystallite size using XRD. *World J. Nano Sci. Eng.* **2012**, *2*, 154–160. [[CrossRef](#)]
32. Mahmood, S.H.; Dushaq, G.H.; Bsoul, I.; Awawdeh, M.A.; Juwhari, H.K.; Lahlouh, B.; AlDamen, M.A. Magnetic properties and hyperfine interactions in M-type $\text{BaFe}_{12-2x}\text{Mo}_x\text{Zn}_x\text{O}_{19}$ hexaferrites. *J. Appl. Math. Phys.* **2014**, *2*, 77–87. [[CrossRef](#)]
33. Li, Y.; Wang, Q.; Yang, H. Synthesis, characterization, and magnetic properties of nanocrystalline $\text{BaFe}_{12}\text{O}_{19}$ Ferrite. *Curr. Appl. Phys.* **2009**, *9*, 1375–1380. [[CrossRef](#)]
34. Trukhanov, S.V.; Trukhanov, A.V.; Kostishyn, V.G.; Panina, L.V.; Trukhanov, A.V.; Turchenko, V.A.; Tishkevich, D.I.; Trukhanova, E.L.; Yakovenko, O.S.; Matzui, L.Y.; et al. Effect of gallium doping on electromagnetic properties of barium hexaferrite. *J. Phys. Chem. Solid.* **2017**, *111*, 142–152. [[CrossRef](#)]
35. Trukhanov, S.V.; Trukhanov, A.V.; Kostishyn, V.G.; Panina, L.V.; Trukhanov, A.V.; Turchenko, V.A.; Tishkevich, D.I.; Trukhanova, E.L.; Yakovenko, O.S.; Matzui, L.Yu. Investigation into the structural features and microwave absorption of doped barium hexaferrites. *Dalton Trans.* **2017**, *46*, 9010–9021. [[CrossRef](#)]
36. Trukhanov, S.V.; Trukhanov, A.V.; Salem, M.M.; Trukhanova, E.L.; Panina, L.V.; Kostishyn, V.G.; Darwish, M.A.; Trukhanov, A.V.; Zubar, T.I.; Tishkevich, D.I.; et al. Preparation and investigation of structure, magnetic and dielectric properties of $(\text{BaFe}_{11.9}\text{Al}_{0.1}\text{O}_{19})_{1-x}(\text{BaTiO}_3)_x$ bicomponent ceramics. *Ceram. Int.* **2018**, *44*, 21295–21302. [[CrossRef](#)]
37. Trukhanov, S.V.; Trukhanov, A.V.; Turchenko, V.A.; Trukhanov, A.V.; Tishkevich, D.I.; Trukhanova, E.L.; Zubar, T.I.; Karpinsky, D.V.; Kostishyn, V.G.; Panina, L.V.; et al. Magnetic and dipole moments in indium doped barium hexaferrites. *J. Magn. Magn. Mater.* **2018**, *457*, 83–96. [[CrossRef](#)]
38. Trukhanov, S.V.; Trukhanov, A.V.; Turchenko, V.A.; Kostishyn, V.G.; Panina, L.V.; Kazakevich, I.S.; Balagurov, A.M. Structure and magnetic properties of $\text{BaFe}_{11.9}\text{In}_{0.1}\text{O}_{19}$ hexaferrite in a wide temperature range. *J. Alloy. Compd.* **2016**, *689*, 383–393. [[CrossRef](#)]
39. Turchenko, V.A.; Trukhanov, S.V.; Balagurov, A.M.; Kostishyn, V.G.; Trukhanov, A.V.; Panina, L.V.; Trukhanova, E.L. Features of crystal structure and dual ferroic properties of $\text{BaFe}_{12-x}\text{Me}_x\text{O}_{19}$ ($\text{Me} = \text{In}^{3+}$ and Ga^{3+} ; $x = 0.1\text{--}1.2$). *J. Magn. Magn. Mater.* **2018**, *464*, 139–147. [[CrossRef](#)]

